Development of Simulation Tools for High-fidelity Analysis of Compound Rotorcraft

T. Zhang*, G. N. Barakos†
CFD Laboratory, School of Engineering, University of Glasgow, G12 8QQ Glasgow, UK.

This paper presents the development and validation of a tool chain for high-fidelity analysis of compound rotorcraft. An automatic geometry composition and grid generation framework is constructed using ICEM Hexa scripts and in-house codes. Simulation methods of various fidelity levels are then put forward and evaluated. The framework is examined and validated through simulations of ducted propeller cases. The high fidelity CFD simulations are performed using the HMB3 solver. Comparisons and validation are made with experimental data, as well as simpler predictive methods. The ducted propeller shows superior performance over its un-ducted counterpart at low or moderate advance ratios. The ducted propeller also shows less intrusive wake features. The major thrust gain is identified to originate from the duct itself. As the advance ratio increases, the duct thrust contribution becomes negative and the ducted propeller thus becomes deficient. Cross-wind conditions are also considered. The duct is found to be the source of the large lift force and the nose-up pitching moment. Detailed analyses of the duct surface pressure and the propeller induction are presented.

Nomenclature

Latin

AoA	=	Angle of Attact, degrees $^\circ$
P	=	Pressure, Pa
V	=	Flow Velocity, m/s
RPM	=	Revolution per Minute
L	=	Lift, N
D	=	Drag, N
T	=	Propeller Thrust, N
R	=	Blade Radius, m
F_x	=	Axial Force, N
M_x	=	Axial Moment, Nm
M	=	Pitching Moment, Nm
Re	=	Reynolds Number, $Re = V_\infty c_{DF}/\nu_\infty$
c_{DF}	=	Duct Chord, m
D_{DF}	=	Duct Exit Diameter, m
S	=	Area, m^2
S_{DF}	=	Ducted Fan Reference Area, $S_{DF} = c_{DF} D_{DF}$, m^2
C_p	=	Pressure Coefficient, $C_p = \frac{P-P_\infty}{0.5\rho_\infty (V_\infty)^2}$
C_T	=	Propeller Thrust Coefficient, $C_T = \frac{T}{0.5\rho_\infty (V_{tip})^2 \pi R^2}$
C_l	=	Lift Coefficient, $C_l = \frac{L}{0.5\rho_\infty (V_\infty)^2 S_{DF}}$
C_d	=	Drag Coefficient, $C_d = \frac{D}{0.5\rho_\infty (V_\infty)^2 S_{DF}}$
C_m	=	Pitching Moment Coefficient, $C_m = \frac{M}{0.5\rho_\infty (V_\infty)^2 S_{DF} c_{DF}}$
C_{F_x}	=	Axial Force Coefficient, $C_{F_x} = \frac{F_x}{0.5\rho_\infty (V_\infty)^2 S_{DF}}$
C_{M_x}	=	Axial Moment Coefficient,$C_{M_x} = \frac{M_x}{0.5\rho_\infty (V_\infty)^2 S_{DF} c_{DF}}$

*PhD Student, CFD Laboratory, School of Engineering, Email: 2354711Z@student.gla.ac.uk
†Professor, MAIAA, MRAeS, CFD Laboratory, School of Engineering, Email: George.Barakos@glasgow.ac.uk

Greek

μ = Advance Ratio, $\mu = \frac{V_\infty}{V_{tip}}$
ν = Kinematic Viscosity, m^2/s

Subscripts and superscripts

∞ = Freestream Value
tip = Blade Tip Value
x = Axial Direction Value
OP = Open Propeller
DF = Ducted Fan
avg = Azimuth Averaged
max = Azimuthal Maximum
min = Azimuthal Minimum

Acronyms

AIAA = American Institute of Aeronautics and Astronautics
NASA = National Aeronautics and Space Administration
CFD = Computational Fluid Dynamics
CAD = Computational Aided Design
MRF = Multiple Reference Frame
DFDC = Ducted Fan Design Code
HMB3 = Helicopter Multi-Block 3
NURBS = Non-Uniform Rational B-Spline
SST = Shear Stress Transport
SAS = Scale Adaptive Simulation
RANS = Reynolds Averaged Navier Stokes

I. Introduction

Conventional helicopters, through compounding [1], can effectively overcome their speed limitations. However, the combination of multiple sources of lift and thrust brings significant challenges in terms of aerodynamic interactions, vibration and stability, control and trim difficulties, power allocation etc. As shown in Figure 2, many attempts at compound helicopter are reported ever since the very early age of vertical flight, but most were discontinued. Less data and few research works can be found in the public domain comparing to conventional helicopters, and significant research and development should be carried out. Nevertheless, a recent resurgence of compound rotorcraft research can be noticed. Flight tests for the coaxial SB>1 Defiant compound are now on the way, and several novel eVTOL configurations are now under development. Experiments on the advanced AH-64 compound has also been reported [2]. High-fidelity simulation campaigns of the RACER compound helicopter in very recent years have also been conducted [3][4][5].

As for the auxiliary thrust, propellers are mostly chosen for their simplicity and efficiency, as seen on the X^3 and the SB>1 Defiant vehicles (Figure 2). However, ducted propellers may represent a better choice of thrust for future compound rotorcraft. By enclosing the propeller with a well-designed annular duct, the combination can deliver higher thrust with the same power at low or moderate speeds. The deployment of ducted propellers can be found in several old and recent designs, as presented in Figures 1(a) to 1(c). The duct also reduces aerodynamic interactions between the propeller and external components. Physical protection to the propeller and ground personnel/equipment may also be seen as advantages. In emergencies, the duct supports containment, preventing further damage to the airframe. Further, by adding guide vanes at the exit, vectorised thrust can be obtained for propulsion or control, as in the Piasecki Pathfinder (Figure 1(a)). Potentially acoustic shielding can also be expected. Nevertheless, few detailed performance investigations of ducted propellers for aircraft applications can be found, especially in off-design conditions like high speed flight and cross-wind conditions.

Simulation methods like CFD are now frequently used for aerodynamic analysis of rotorcraft. The simulation of

(a) Piasecki Pathfinder

(b) Coaxial Compound Helicopter (CCH) by Johnson[6]

(c) Bell Nexus eVTOL air taxi.

Fig. 1 Ducted fan for compound helicopter applications.

novel compound rotorcraft, however, often involves various components of complex geometries and moving parts, and potentially excessive aerodynamic interactions. To reach the necessary efficiency for further analysis and optimisation, modelling options, and tool chain development for the pre-/post-processing of modern and future CFD methods must be put forward.

This work presents the tool chain development and validation for the further high-fidelity analysis of compound rotorcraft. An automatic geometry composition and grid generation framework for various components is constructed using ICEM Hexa scripts and in-house computer codes. The framework is examined and validated through simulations of various ducted propeller cases. High fidelity CFD simulations are performed using the HMB3 solver. Comparisons and validation are made with experimental data, as well as simpler predictive methods. Ducted propeller performance is calculated and analysed with variations of advance ratio and angle of attack.

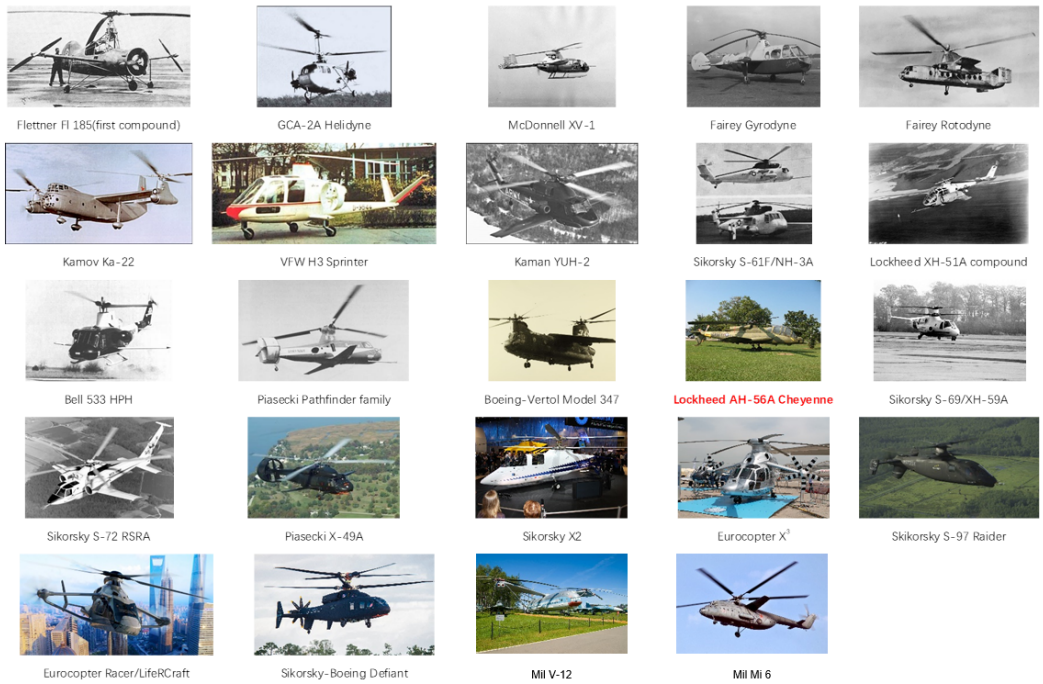

Fig. 2 Compound helicopters as advanced prototypes or at design stages.

II. Tool Chain Development

Simulations and analyses of various configurations and geometries are necessary to study the general aerodynamic interactions among different components of a compound rotorcraft, and eventually to determine the optimal aerodynamic design subject to applied constraints. A flowchart of the aerodynamic analysis process is presented in Figure 3. The procedure involves the handling of complex geometries and grid generation, which often demands large amount of

human interactions. In addition, aerodynamic modelling methods of various fidelity levels need to be put forward for the necessary efficiency. To facilitate the analysis process and reduce the workload, a tool chain is therefore proposed. The tool chain consists of an automatic grid generation framework, the in-house HMB3 CFD solver, lower-order analysis packages for ducted and un-ducted propellers, and shell scripts for further automation.

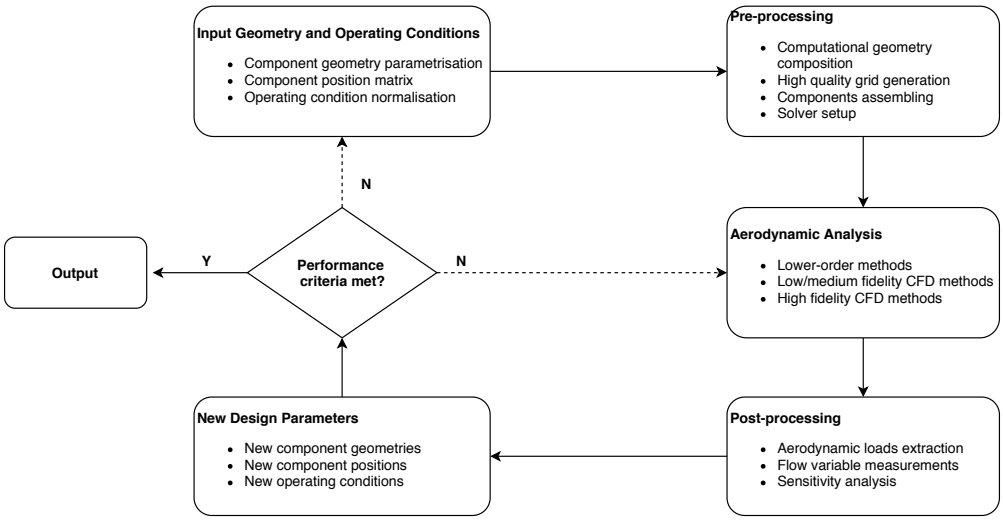

Fig. 3 Flow-chart of compound rotorcraft simulation and analysis process.

A. Automatic Grid Generation Framework

As a key part of CFD analyses and optimisation, mesh generation demands a significant amount of effort and human interaction. While for the analysis of compound rotorcraft, simulations are needed for various components of variable shapes. An automation framework for geometry composition and grid generation is therefore proposed in the present work using the ICEM Hexa mesher. The ICEM Hexa mesher is a commercial package for the generation of structured, hexahedral, and body-fitted grids. It is incorporated with a Tcl/Tl shell interface with an extended library of commands, so that automation can be realised through high-level programming.

The proposed automation framework is designed to deliver not only ready-to-run, multi-block, structured grids for CFD solvers, but also geometry models for CAD tools, all from a given set of parameters. Comparing to many in-house automatic grid generation codes, the framework features a high degree of versatility and simplicity for distinct shapes. File compatibility for many CAE tools in terms of both input and output is also ensured.

A schematic of the current framework is presented in Figure 4. The framework is implemented using in-house codes, ICEM Hexa scripts, and Unix shell scripts. Through in-house pre-processing codes, the input geometry is analysed and parametrised. Definitive features, like sectional profiles, are extracted and exported in ICEM-compatible formats. Parameters governing the geometry generation, as well as, the meshing process, e.g. outer boundary size, nodes bunching, are taken as input.

With parameters defined, scripts for different shape patterns, e.g. blade/wing, fuselage, or duct, are then executed by ICEM. Modules of the ICEM scripts are presented in Figure 5. NURBS based geometries are composed using the geometry module of ICEM Hexa. The blocking process, a major part of the mesh generation that needs extensive human interaction, is realised by importing pre-defined and robust mesh topologies. The design of these topologies for particular applications still needs human effort in advance, but block vertices, edges, and faces are handled by the scripts, according to the specific geometry and the parameters input. The post-processing codes convert the output to CFD solvers and external CAD tools.

A sample blade geometry is presented in Figure 6. The framework delivers good flexibility and versatility for variations of e.g. aspect ratio, twist distribution, swept/anhedral, and sectional shapes. The span-wise and sectional outlines are represented using B-splines. Piece-wise NURBS surfaces are then composed based on the wireframe. Geometric smoothness for computational grid generation can be ensured given smooth input sectional profiles and parameters.

The framework is also tested using distinct duct shapes with the thick NACA0050 profile (Figure 7(a)) and the highly

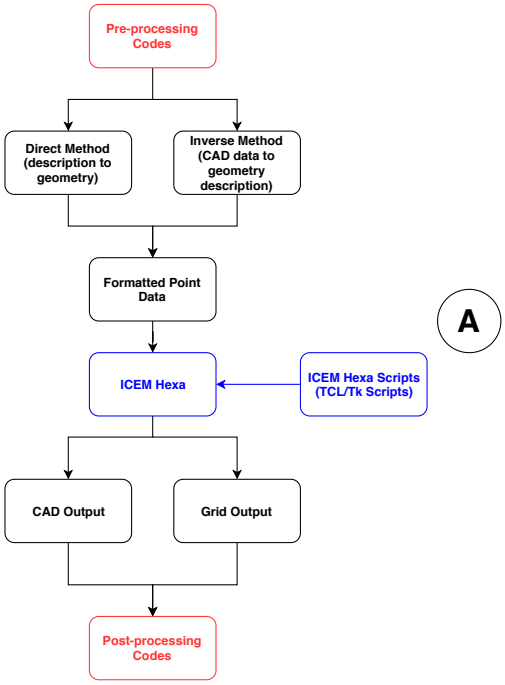

Fig. 4 Flow-chart of the automation framework for geometry composition and mesh generation.

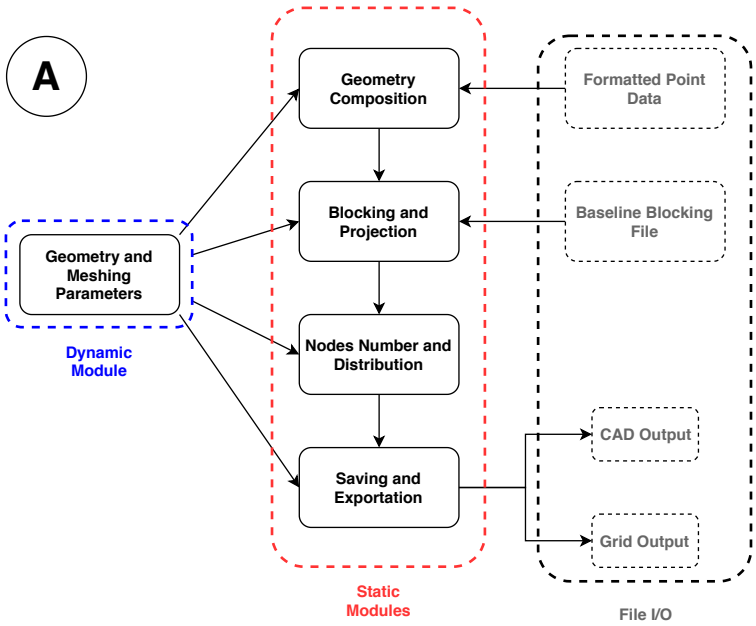

Fig. 5 Modules of the ICEM Hexa scripts embedded in the automation framework (module A in Figure 4).

cambered, thin NACA8406 7(b) profile. The grids can afterwards be assembled using Chimera methods from a correct set of transformational parameters as shown in Figures 8(a) and 8(b). Alternative grid topologies for fully-matched grids for duct/centre-body combinations are also implemented as shown in Figure 7(c). Asymmetric duct geometries, shown in Figure 8(c), are also supported. With the help of the automation framework, the time needed for the geometry composition and high-quality grid generation can be reduced from hours to less than a minute. It is therefore enabled to quickly generate a large library of shapes for systematic study or optimisation.

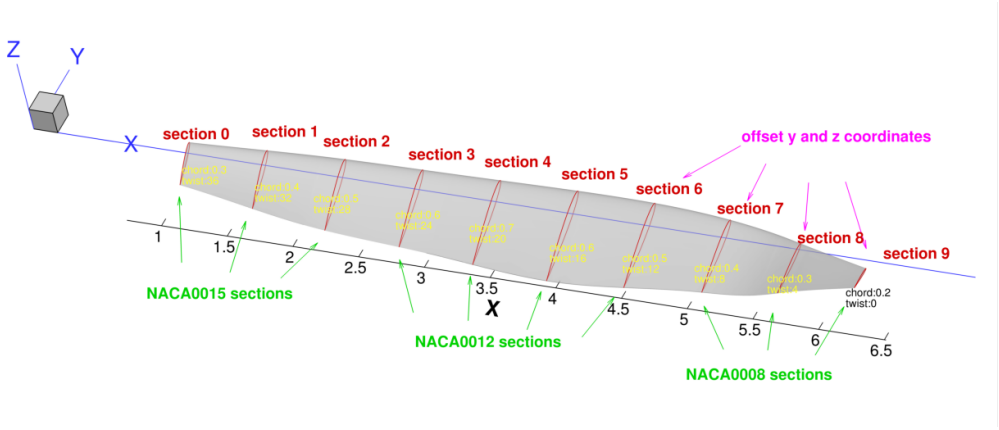

Fig. 6 Sample blade geometry composed by the framework with sections of variable shapes, chord length, local twist angles, and offset in swept and anhedral/dihedral directions.

B. HMB3 Solver

The Helicopter Multi-Block (HMB3) [9–11] code is used in the present work. HMB3 solves the Unsteady Reynolds Averaged Navier-Stokes (URANS) equations in integral form using the Arbitrary Lagrangian Eulerian (ALE) formulation for time-dependent domains, which may include moving boundaries. The Navier-Stokes equations are discretised using a cell-centred finite volume approach on a multi-block grid. The spatial discretisation of these equations leads to a set of ordinary differential equations in the temporal domain.

$$\frac{d}{dt}\left(\mathbf{W}_{i,j,k}V_{i,j,k}\right) = -\mathbf{R}_{i,j,k}\left(\mathbf{W}_{i,j,k}\right), \tag{1}$$

where i,j,k represent the cell index, $\mathbf{W}$ and $\mathbf{R}$ are the vector of conservative flow variables and flux residual respectively, and $V_{i,j,k}$ is the volume of the cell i,j,k. To evaluate the convective fluxes, Osher [12] approximate Riemman solver is used, while the viscous terms are discretised using a second order central difference scheme. The MUSCL (Monotone Upstream-centered Schemes for Conservation Laws) approach developed by Leer [13] is used to provide high-order accuracy in space. The HMB3 solver uses the alternative form of the Albada limiter [14] in regions where large gradients are encountered mainly due to shock waves, avoiding the non-physical spurious oscillations. An implicit dual-time stepping method is employed to perform the temporal integration, where the solution is marching in pseudo-time iterations to achieve a fast convergence. The linearised system of equations is solved using the Generalised Conjugate Gradient method with a Block Incomplete Lower-Upper (BILU) factorisation as a pre-conditioner [15]. Multi-block structured grids allow for the easy balancing of calculation load of high performance parallel computing.

Various turbulence modelling methods are available in the HMB3 solver, including several one-equation, two-equation, three-equation, and four-equation turbulence models. Furthermore, Large-Eddy simulation (LES), Detached-Eddy Simulation (DES), and Delayed-Detached-Eddy Simulation (DDES) are also available. In the present work the $k-\omega$ SST [16] turbulence model and the Scale Adaptive Simulation (SAS) method are used, considering the possibly excessive separation. The SAS formulation adds an additional source term to the $k-\omega$ SST equations, which allows the local adjustment of the von Karman length scale and balances contributions from the resolved and statistical components. The SAS implementation in HMB3 has been used for studies of cavity flows [17], missile projection [18], and stall flutter [19].

The HMB3 solver is also equipped with variable mesh methods. It is enabled to handle multi-block, structured grids with sliding planes [10], Chimera overset grids [20], and unstructured grids [21]. The Chimera method is extensively

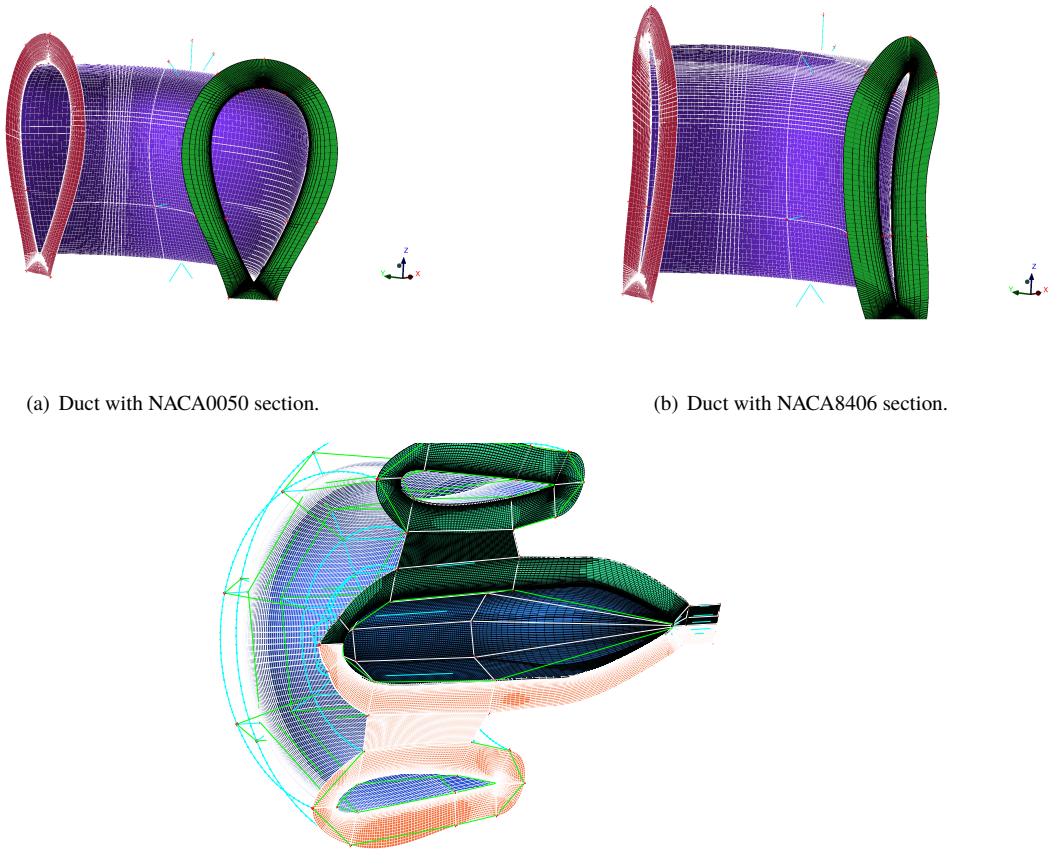

(a) Duct with NACA0050 section.

(b) Duct with NACA8406 section.

(c) Combined duct and centre-body geometry and grid topology.
The case corresponds to the experiments of Hubbard[7].

Fig. 7 Different duct shapes using NACA0050 and NACA8406 airfoils as sections, and alternative grid topology for duct and centre-body combinations.

used in this work, as it simplifies the grid generation and allows relative motions between grids. The flexibility of adding/removing components, or changing component positions is also ensured. As mentioned earlier, the multi-block, structured grids for each component, generated by the automation framework, are assembled and calculated using the Chimera method.

The Multiple Reference Frame (MRF) method is also implemented [22] for simulations with rotational periodicity, such as rotors in hover or axial flight. The HMB3 solver is enabled to solve the governing equations formulated in a non-inertial and rotating reference frame, which converts the unsteady problem into steady calculations. With the help of periodic boundaries, only a fraction of the whole computational domain needs to be considered, thereby significantly reducing the computational cost. Stationary wall boundaries with respect to rotating rotors, e.g. ducts, can also be accounted for by imposing opposite motions. This strategy is adopted in the simulation of ducted propellers in hover and axial flight.

C. XRotor and DFDC Codes

The XRotor and DFDC (Ducted Fan Design Codes) are open-source tools developed by Drela et.al. [23–25] for the performance prediction and design of ducted/un-ducted propellers. The codes are based on extended classic blade-element/vortex theories, in combination with lifting line and panel methods. They are capable of quickly predicting, or matching the performance for specific geometries, as well as solving the inverse design problem. The

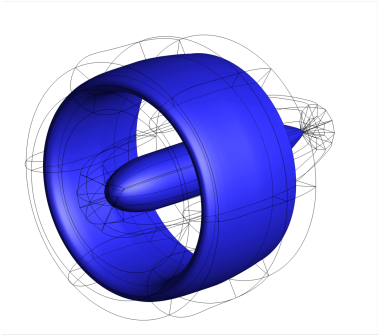

(a) Mesh topology of an empty ducted fan. The case corresponds to the experiments of Grunwald *et al.* [8]

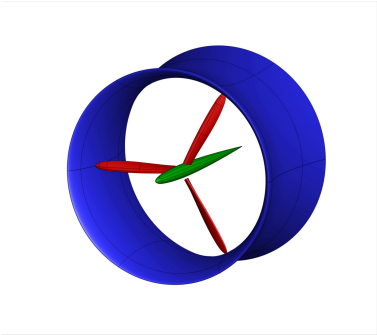

(b) Transformed and assembled ducted fan components.

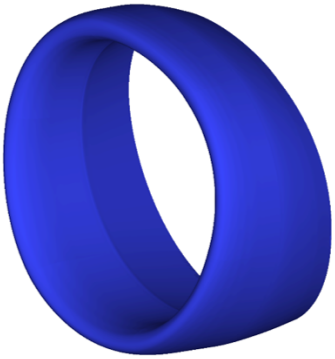

(c) Asymetric duct shape.

Fig. 8 Assembled grid topologies and geometries.

codes take as input the duct and centre-body geometries, and airfoil tables for propeller sections. However, only axisymmetric conditions, e.g. hover or axial flight can be accounted for. The XRotor and DFDC codes are used in this work for comparisons with HMB3 results.

III. Tool Chain Validation

A. Test Matrix

To validate the proposed automation framework and the HMB3 methods, two ducted propeller test cases [7][8] by NASA are used. The cases are chosen for their favourable scales and Reynolds numbers, and also the elaborate geometry information and experimental data. Apart from the experimental conditions for validation, off-design operating conditions are also explored and presented in the following sections to investigate the performance limitations. Detailed test conditions are listed in Table 1. The variables considered include advance ratios and free-stream directions. The advance ratio in MRF simulations (axial cases) is changed by altering the free-stream speed, while maintaining the same blade tip speed and Reynolds number (based on tip speed and duct chord length). Comparisons are also made against un-ducted propellers working at the same axial conditions. Due to the lack of detailed experimental data, the DFDC and XRotor [23–25] codes are also utilised for validation and comparisons in axial conditions.

B. Geometry and Grids

Computational grids are generated using the proposed automation framework for each component and assembled using Chimera methods. Grid topologies for hover and axial flight simulations are presented in Figures 9(a) and 9(b).

Table 1 Test Matrix for Ducted Fan Validation and Analysis

Case	Configuration	Freestream Vel (m/s)	mu	Angle 1 (°)	Angle 2 (°)	Angle 3 (°)	No. Blades	Tip Clearence (mm)	Rot Speed (RPM)	Tip Mach
1	Empty Grunwald	30.48	-		0 to 30		-	-	-	-
2	Grunwald	30.48	0.19	0.00	20.00	50.00	3	1.016	8000	0.4694
3	Hubbard - Shroud B	0.00	0.00	-	-	-	2	2.38	3300	-
4	Hubbard - Shroud B	0.00	0.00	-	-	-	2	6.1	3300	-
5	Hubbard - Shroud B	0.00	0.00	-	-	-	2	12.2	3300	-
6	Grunwald	0.00	0.00	-	-	-	3	1.016	8000	0.4694
7	Grunwald	15.00	0.10	0.00	20.00	90.00	3	1.016	8000	0.4694
8	Grunwald	60.00	0.38	0.00	20.00	50.00	3	1.016	8000	0.4694
9	Grunwald	72.54	0.45	0.00	45.00	90.00	3	1.016	8000	0.4694
10	Grunwald	82.30	0.52	0.00	45.00	90.00	3	1.016	8000	0.4694
11	Grunwald	102.88	0.64	0.00	45.00	90.00	3	1.016	8000	0.4694
12	Hubbard - Shroud B	50.00	0.25	-	-	-	2	2.38	3300	0.6

For hover and axial flight simulations, the Multiple Reference Frame (MRF) method, as described in Section III.B, is used. The unsteady but periodic hover and axial flight cases are therefore converted into steady calculations on a fraction of the entire domain.

For simulations in cross-wind conditions, however, complete configurations are used and the blade motions have to be resolved fully. Complete grids are obtained by copying and rotating the periodic grids. Grid topologies for the empty, and the complete un-ducted/ducted propellers simulations are presented in Figures 10(a), 10(b), and 10(c), respectively. Note the small tip and root clearance between the blade and the duct/centre-body are kept in accordance with experiments and resolved using Chimera methods.

C. Results and Comparisons

Empty Grunwald Duct

Simulations are first performed on the empty Grunwald [8] duct at increasing pitch angles without the propeller. Simulations are performed using steady RANS methods at low AoA and unsteady SAS methods at higher, where massive separation is present on the up-stream inner surface and the down-stream outer surface. Plots of the lift and drag variations with AoA are presented in Figures 11(a) and 11(b).

As shown in Figure 11(a), lift coefficients derived from the steady simulations are in good agreement with experimental data, until high AoA. The empty duct behaves like an annular wing [26] with the propeller removed. Separation is expected on the up-stream inner and the down-stream outer surfaces at high incidences. The steady simulations significantly overpredict the lift at high angles of attack, where stall is expected. The drag coefficients from steady calculations are slightly overpredicted comparing to the experiments, nevertheless the trend is well predicted.

Unsteady simulations are performed at high incidences and the results are also plotted in Figures 11(a) and 11(b). Through the unsteady SAS methods, the unsteady separation is resolved and better agreement in aerodynamic loads with experiments is achieved. The non-dimensional y-vorticity contours on the middle plane (Y=0) are presented in Figures 13(a) to 13(c) for $AoA = 20°, 25°, 30°$, respectively. Flow separation arises from the increasing AoA, first at the upstream diffuser exit, especially after the abrupt geometry expansion where a sudden adverse pressure gradient should be seen. As the AoA further increases, as shown in Figures 13(b) at $AoA = 25°$ and 13(c) at $AoA = 30°$, complex separation dominates the entire inner upstream surface starting from the leading edge. Large separation is also seen on the downstream outer surface. At $AoA = 30°$, the wake of the upstream separation is also hitting the centre-body surface, creating more complex secondary flows. Overall the empty duct at high AoA sees very complex stall conditions, yet the resolution of such flows is within the capability of modern CFD methods.

The axial velocity profiles (normalised by free-stream speed) right above the rotor disk are presented in Figures 12(a) and 12(b) for incidences of 0° and 20°, respectively. Due to the induction of the duct, at $AoA = 0°$, the propeller sees a 30% higher baseline inflow velocity for the case simulated. The radial speed distribution is almost even, with slightly higher values positioned near the duct inner surface. For the cross-wind condition (Figure 12(b)), the propeller experiences an imbalanced inflow profile. This is discussed further in Section V.

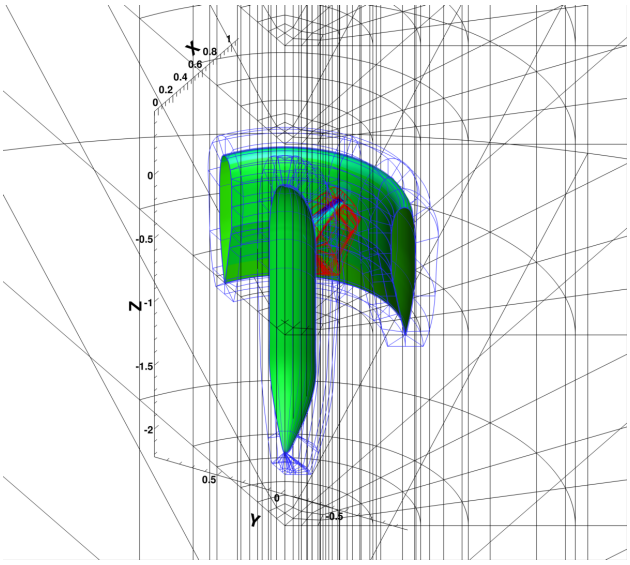

(a) Three-bladed Grunwal ducted propeller [8] grid topologies for MRF simulations.

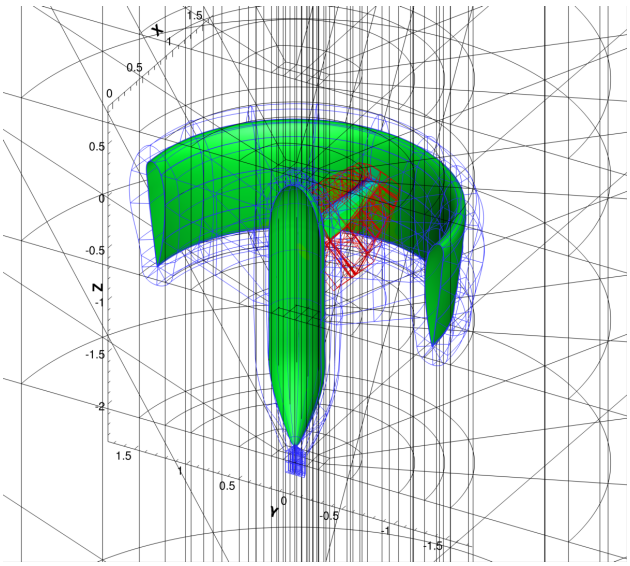

(b) Two-bladed Hubbard ducted propeller [7] grid topologies for MRF simulations.

Fig. 9 Multi-block grid topologies for ducted propeller simulations using Multiple Reference Frame (MRF) methods.

Grunwald Ducted Propeller

Comparisons for the complete ducted fan configuration, between experiments and HMB3 simulations in axial flight, as well as the breakdown of propulsion forces, are listed in Table 2 and shown in Figure 14, and good agreement can be noticed between CFD, simpler predictive methods [23][24][25] and the test data. For the convenience of comparing, all force and moment data are normalised using the far-field dynamic pressure, the duct chord length C_{df}, and the projected duct area S_{df}.

Results using the DFDC code [24][25] are obtained by matching the overall thrust. This results in a $\theta_{0.7}$ of 29.58° under the same RPM, far-field speed and geometries. The same pitch setting is also applied in the CFD simulations. Figures 15(a) and 15(b) show good correlation between the methods for averaged pressure distributions along the centre-body and duct. Relative differences with respect to the experimental results are presented in Table 3 and Figure

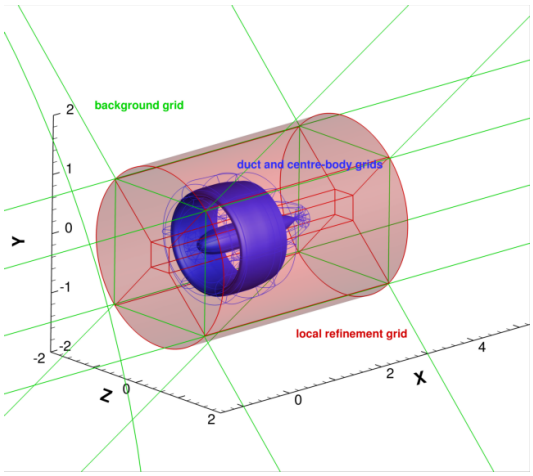

(a) Geometry and grid topology of the empty duct case.

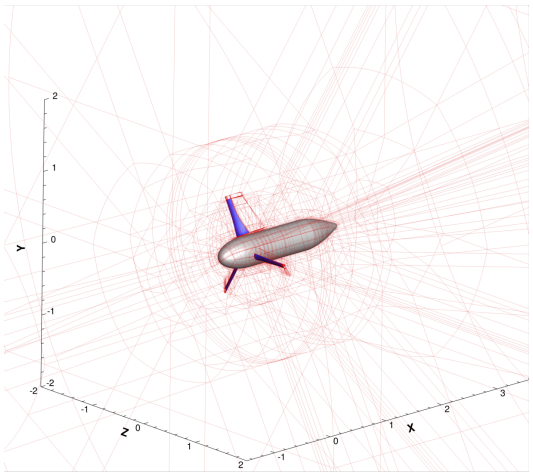

(b) Geometry and grid topology of the complete un-ducted propeller case.

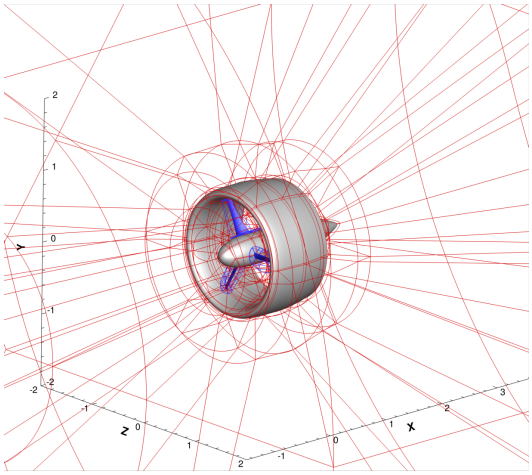

(c) Geometry and grid topology of the complete ducted propeller case.

Fig. 10 Geometries, multi-block mesh topologies, and the coordinate systems of the Grunwald [8] configurations.

16. It can be noted that differences between the HMB3 results and the experiments are minor in this case.

Table 2 Aerodynamic loads breakdown and comparisons between experiments, HMB3 simulations and simpler predictive methods.

C_{Fx}	EXP	Contribution	DFDC	Contribution	HMB3	Contribution	HMB3_OP	Contribution	XRotor_OP
Total	1.40	100%	1.416	100%	1.396	100%	1.355	100%	1.39
Rotor	1.00	71.4%	0.912	64.4%	0.985	70.6%	1.418	104.7%	1.39
Duct(with CB)	0.40	28.5%	0.504	35.6%	0.410	29.4%	-	-	-
Centre-body	-	-	-	-	0.068	4.9%	-0.063	-4.7%	-
Propeller C_{Mx}	0.27	-	0.391	-	0.279	-	0.313	-	0.391
Efficiency η	0.713	-	0.498	-	0.687	-	0.594	-	0.489

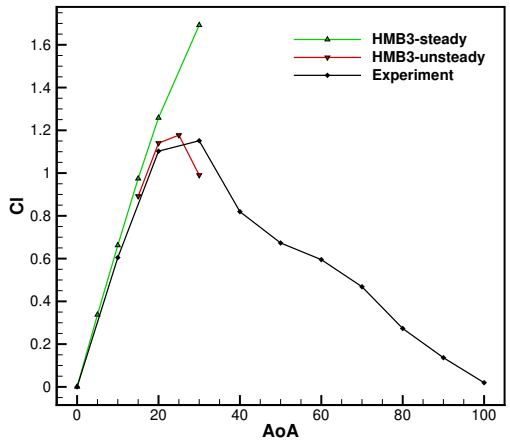

(a) Lift coefficient variations with AoA for the empty Grunwald duct.

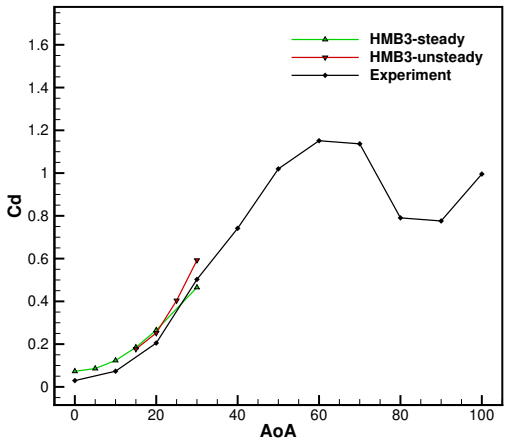

(b) Drag coefficient variations with AoA for the empty Grunwald duct.

Fig. 11 Aerodynamic force variations with increasing AoA for the empty Grunwald duct.

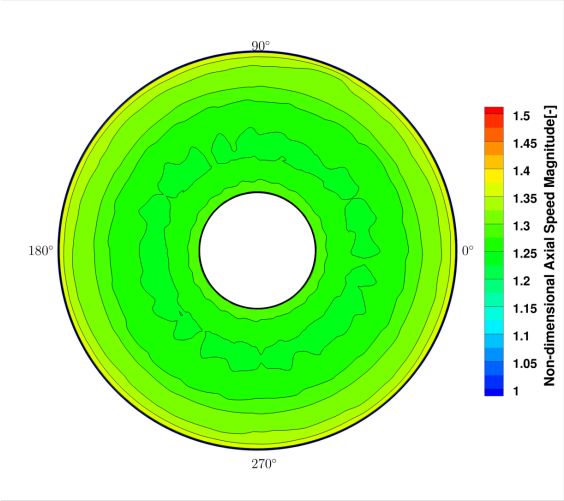

(a) Axial induction factor (normalised by free-stream speed) contours before the rotor disk of the empty duct simulation at $AoA = 0°$.

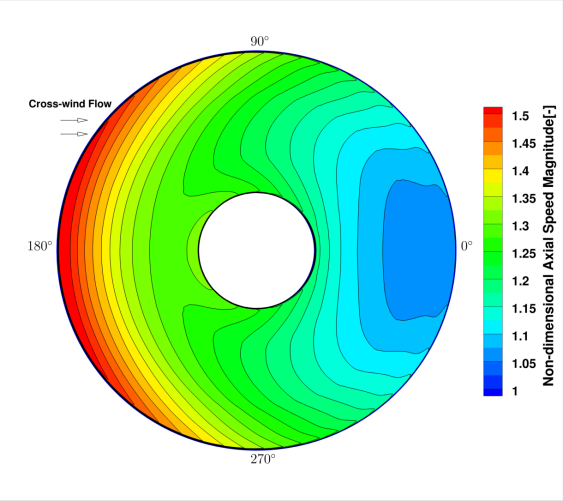

(b) Axial induction factor (normalised by free-stream speed) contours before the rotor disk of the empty duct simulation at $AoA = 20°$.

Fig. 12 Inflow velocity profiles for the rotor disk induced by the empty duct.

Hubbard Ducted Propeller

During the experiments by Hubbard [7], few loads measurements were made as the study mostly focused on acoustics. The duct thrust was integrated from surface pressure tap data, while the propeller thrust was not measured. The propeller torque was estimated from the power consumption from electricity meters. Comparisons of the thrust breakdown between experimental, HMB3, and DFDC results are listed in Table 4.

The pressure coefficient distribution on the duct surface, extracted from the HMB3 simulations, is presented in Figure 17, along with DFDC results. Very good agreement is observed for the outer surface, while for the inner surface the agreement is also favourable.

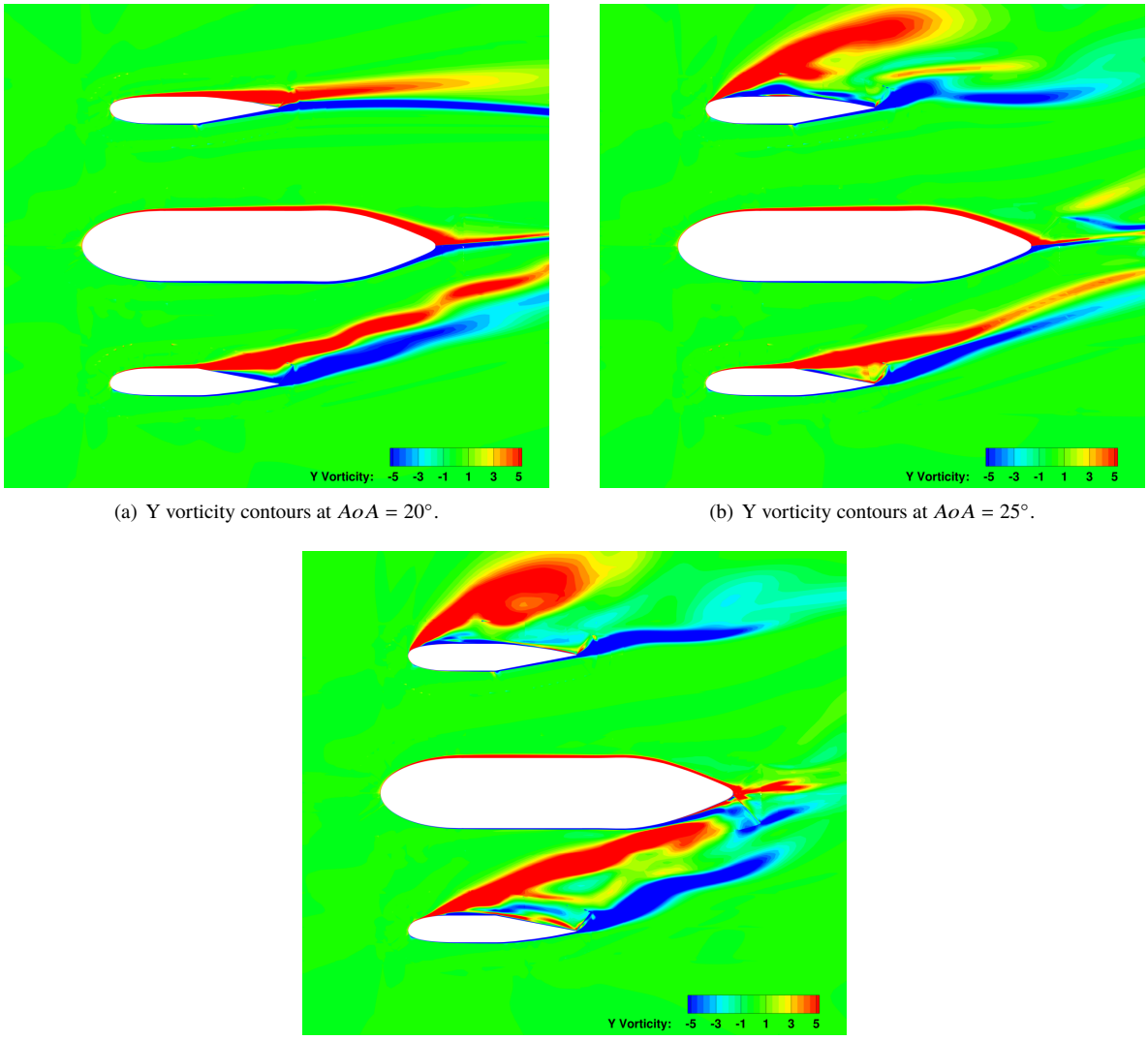

(a) Y vorticity contours at $AoA = 20°$.

(b) Y vorticity contours at $AoA = 25°$.

(c) Y vorticity contours at $AoA = 30°$.

Fig. 13 Flow visualisation on the middle plane (Y=0) for the empty Grunwald duct at $AoA = 20°, 25°, 30°$.

Table 3 Relative error analysis of DFDC and HMB3 predictions ($ERROR = \frac{[Prediction]-[EXP]}{[EXP]}$)

C_{Fx}	EXP	DFDC	ERROR	HMB3	ERROR
Total	1.40	1.416	1.14%	1.396	-0.32%
Rotor	1.00	0.912	-8.80%	0.985	-1.47%
Duct(with CB)	0.40	0.504	26.00%	0.410	2.56%
Centre-body	-	-	-	0.068	-
Propeller C_{Mx}	0.27	0.391	44.81%	0.279	3.35%

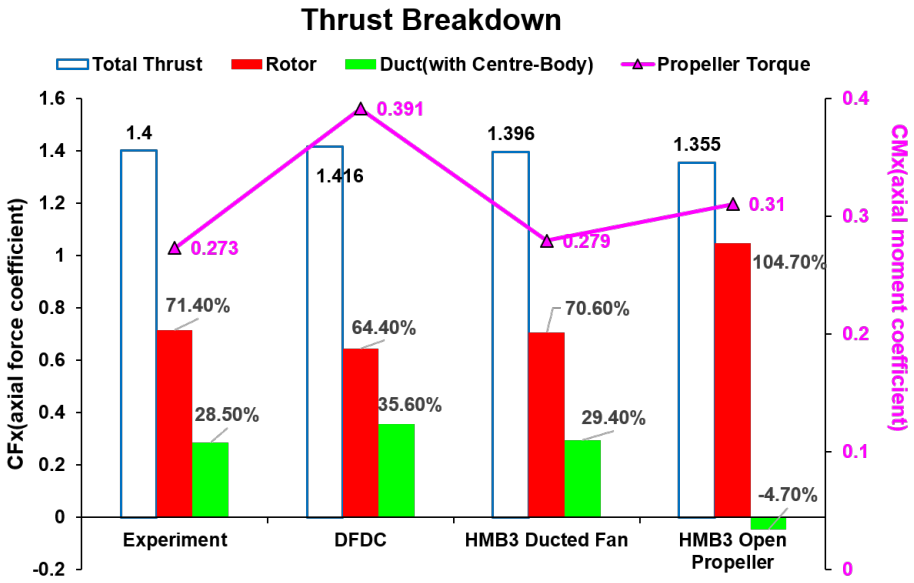

Fig. 14 Aerodynamic load breakdown of the Grunwald [8] ducted propeller HMB3 simulation at $\mu = 0.191$ and comparisons with experiments and DFDC results.

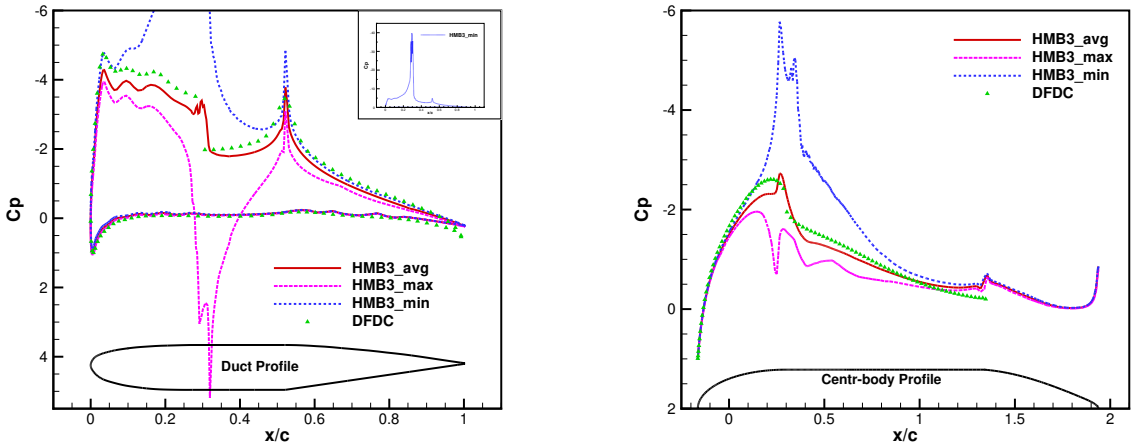

(a) Cp distribution on the duct

(b) Cp distribution on the center-body

Fig. 15 Pressure coefficient distributions along the duct and center-body surface. The peak and averaged values predicted by HMB3 are compared with the method of M. Drela[24][25].

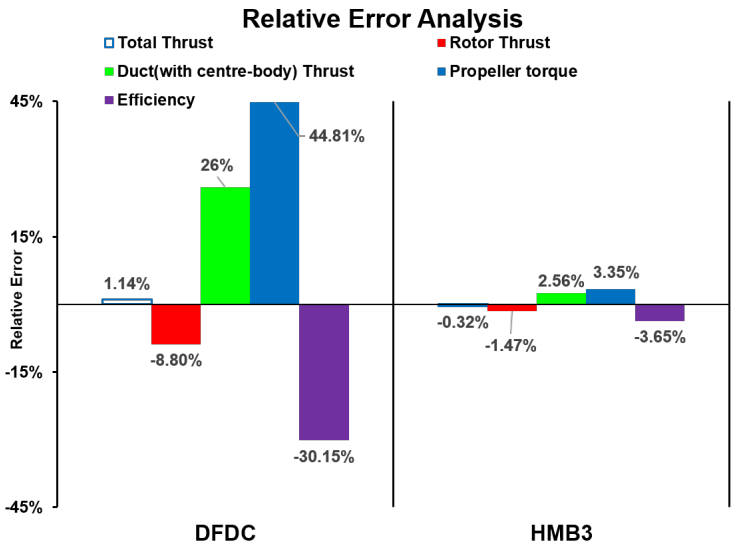

Fig. 16 Relative error analysis with respect to experimental data of DFDC and HMB3 predictions for the Grunwald [8] ducted propeller at $\mu = 0.191$.

Table 4 Comparisons between experiments, HMB3 simulations, and DFDC calculations for the Hubbard ducted fan (values normalised using blade tip speed and disk area).

	Experiments	HMB3	DFDC
Total	-	0.0593	0.0687
Propeller	-	0.0283	0.0334
Duct	0.0317	0.0307	-
Duct+Centre-body	-	0.0310	0.0352
Propeller Torque	0.00748	0.00633	0.00688

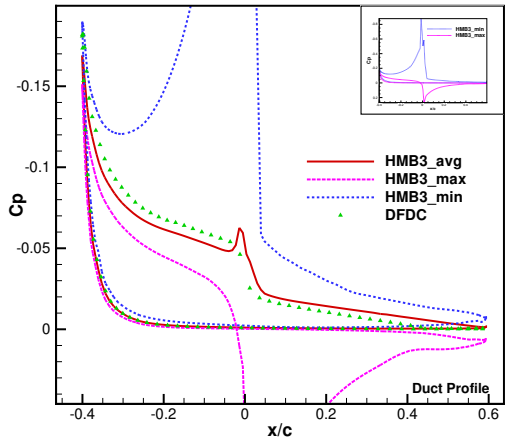

Fig. 17 Surface pressure coefficient (normalised by blade tip speed) comparisons between HMB3 and DFDC results for the Hubbard ducted propeller.

IV. Ducted Propeller Performance Analysis

Further performance analyses and comparisons for the Grunwald ducted propeller [8] are also made against the un-ducted propeller configuration, working at the same RPM and free-stream velocities. Since no open propeller tests were conducted during experiments [8], comparisons are made against XRotor [23] calculations as presented in Table 2. The aerodynamic loads from the HMB3 and XRotor codes are in good correlation with a difference of 2.6% for axial (propulsive) forces.

To examine the suitability of the ducted propeller as auxiliary propulsion for future compound rotorcraft, performance at off-design conditions are also investigated and discussed in this section. The advance ratio range in axial flight is extended to explore the performance at low and high speeds. Non-axial conditions were also calculated to examine the behaviour at cross-wind.

A. Comparions with Un-ducted Propeller in Axial Flight

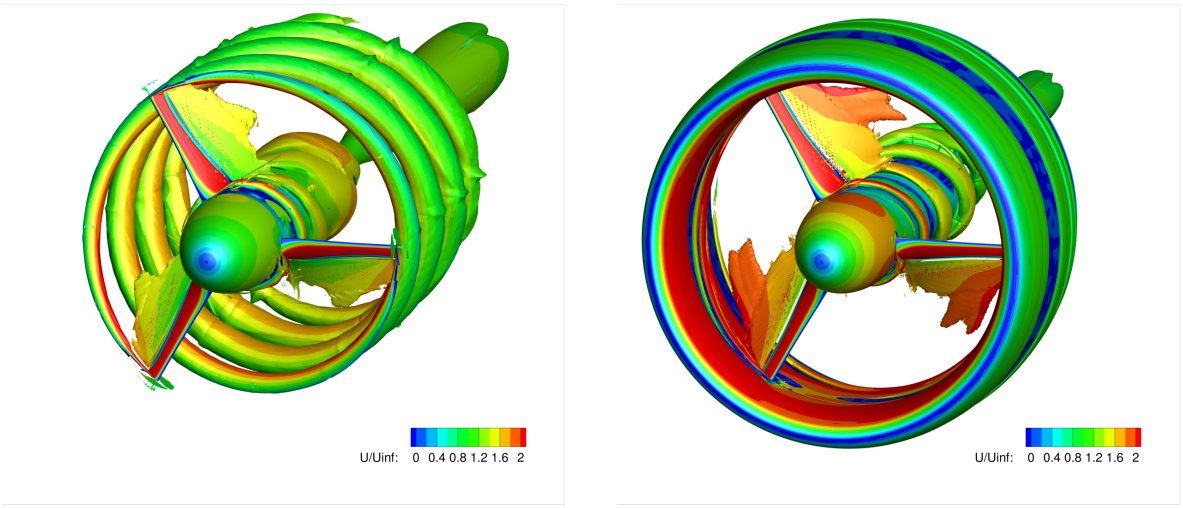

(a) Open propeller (b) Ducted propeller

Fig. 18 Iso-surfaces of non-dimensional Q=5, colored with non-dimensional axial speed.

It can be clearly seen from Figures 18(a) and 18(b) that the presence of the duct significantly suppressed the extent of tip vortices. Further, as shown in Figures 19(a) and 19(d), the inflow is accelerated by the duct curvature at the inlet, leading to the lower regional static pressure. This causes the blades to work at higher inflow velocities. The axial mass and momentum flow rates measured at the diffuser exit for all configurations are presented in Table 5. The presence of the duct increases both the mass and the momentum flow rates for the case calculated. The same result can be expected from simple momentum theory analyses, considering the forcedly expansion of the wake due to the diffuser exit. The increase in mass and momentum flow rates can also be regarded as induced by the duct circulation, similar to that of an annular wing.

Due to the expanded exit area, the ducted propeller produces less intrusive wakes. The axial velocity magnitude measurements, extracted from the ducted and un-ducted simulations, are presented in Figures 20(a) and 20(b). As presented in Figure 20(a), mean values of the axial speed magnitude in the wake vary only slightly as the flow moves further downstream for both cases, whereas the ducted propeller shows a lower averaged axial speed level. Also shown in Figure 20(a) are sectional speed contours at two different stream-wise sections. From the comparison it can be seen that the ducted propeller has a more averaged speed distribution over the section. Also shown in Figure 20(b) is the comparison of axial velocity profiles in the wake. The ducted propeller shows not only lower azimuth-averaged values along the radial direction, but also less fluctuation in the velocity over azimuth. Overall, the ducted propeller is shown to possess less intrusive and more smooth wake features over its un-ducted counter part for the case studied.

To further verify the contribution of the duct, the pressure coefficient distribution and surface pressure vectors at $\mu = 0.191$ are presented in Figure 22(b). It is clearly shown that the leading edge suction, and the higher pressure at the diffuser together contribute to the thrust gain of the ducted propeller. The propeller suction significantly decreases the

Table 5 Axial mass and momentum flow rates measured in HMB3 simulations for the ducted and un-ducted propellers at $\mu = 0.191$, integrated over the diffuser exit section (see Figures 19(a) and 19(d)).

Configuration	Axial mass flow rate $\dot{m}$	Axial momentum flow rate $\dot{m}u$
Open propeller	1.363	1.946
Ducted fan	1.439	2.139

pressure on the inner side of the duct, especially at the inner side leading edge before the rotor disk, where the suction forces reside. A pressure jump is caused by the rotor disk. A low pressure peak limited to a very small area can be observed due to the sudden transition of the geometry at the diffuser. The static pressure is then gradually recovered by the diffuser. Pressure changes on the duct outer surface are little. Overall, the pressure forms a slightly inwards force that has an axial component as propulsion.

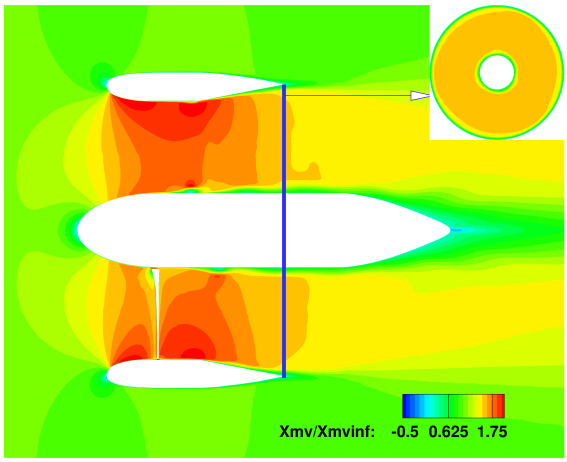

(a) Ducted propeller axial momentum.

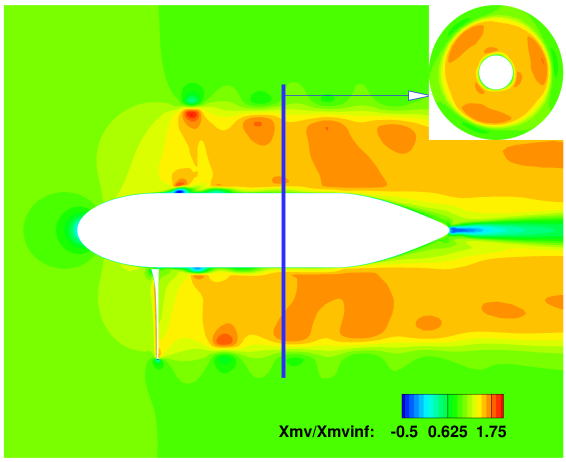

(b) Open propeller axial momentum.

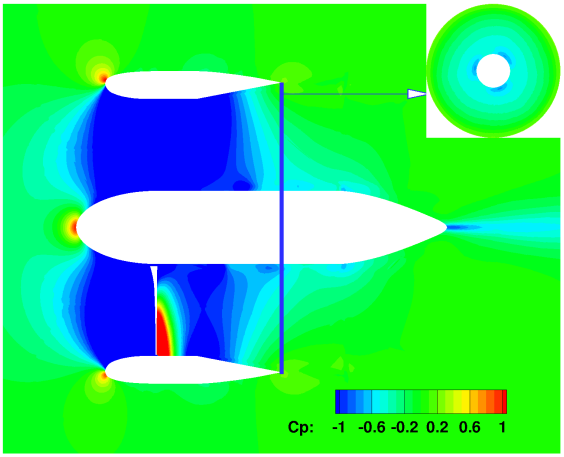

(c) Ducted propeller instantaneous pressure coefficient contours.

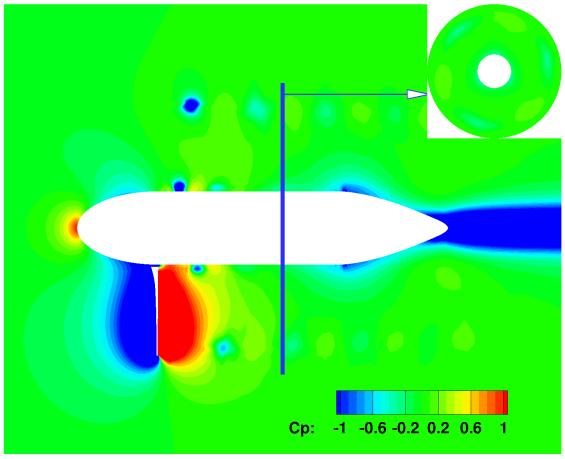

(d) Open propeller instantaneous pressure coefficient contours.

Fig. 19 Axial momentum (normalised by the far-field axial momentum) and instantaneous pressure coefficient comparisons between the ducted propeller and the open propeller ($\mu = 0.191$). Thick blue lines denote the diffuser exit sections.

It can also be noted that the torque produced by the open propeller is higher due to the larger induced drag. As shown in Table 6, torque contributions from the duct and the centre-body are minor. Nevertheless, the overall thrust

of the ducted fan is higher, indicating the superior efficiency of ducted fans as presented in Table 2. Although the performance improvement is moderate due to the high advance ratio in this case.

Table 6 Axial moments breakdown for the Grunwald [8] ducted fan and the open propeller at $\mu = 0.191$.

C_{Mx}	HMB3$_{df}$	Contribution	HMB3$_{op}$	Contribution
Total	0.282	100%	0.314	100%
Rotor	0.279	99.07%	0.313	99.8%
Duct	0.0027	0.96%	-	-

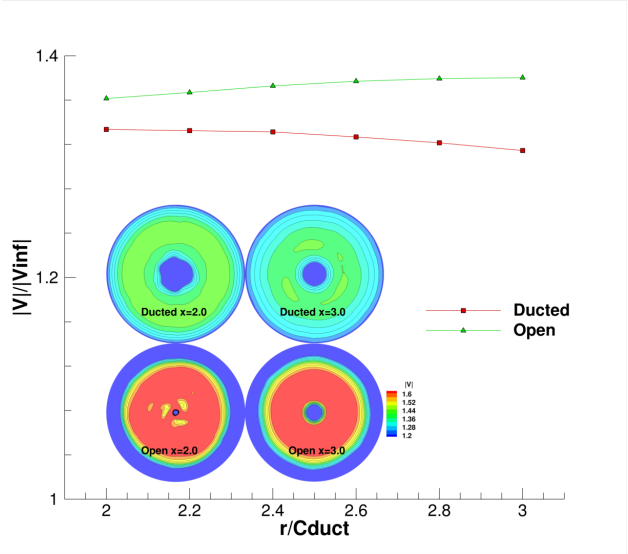

(a) Wake strength comparisons of the ducted and un-ducted propellers.

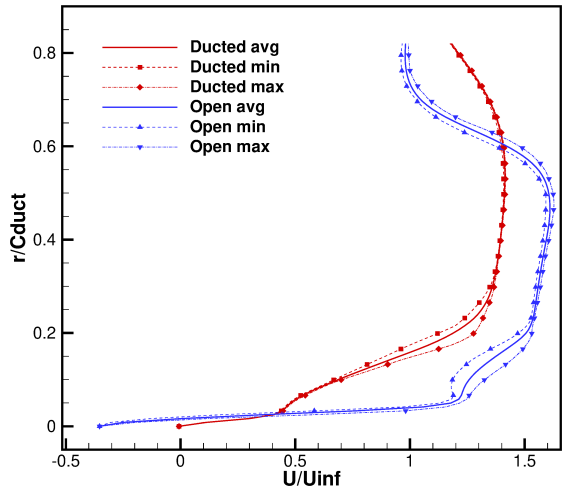

(b) Axial velocity profile comparisons of the ducted and un-ducted propellers.

Fig. 20 Wake comparisons of the ducted and un-ducted propellers.

B. Effects of Advance Ratio on Ducted Propeller Performance

As investigated by several previous experiments and calculations [22][27][28], the efficiency of the ducted propeller drops as the advance ratio increases. The ratio of the propeller thrust to total propulsion increases in the mean time, indicating the deficiency of the duct at high advance ratio. In this light, the advance ratio in axial flight of the ducted propeller studied in this work is extended, ranging from 0.0 (hover) to 0.6447. The advance ratio is changed by changing the free-stream speed, while maintaining the same propeller RPM.

The thrust breakdown of HMB3 and DFDC results at increasing advance ratios is plotted in Figure 21. Experimental data is available for validation only for $\mu = 0.0$ and $\mu = 0.191$, nevertheless good correlation with HMB3 results is seen in both cases. The DFDC calculations are also in favourable agreement with HMB3 simulations, especially at lower advance ratios. Figure 21 shows that as the advance ratio grows, the thrust produced by each component drops gradually and soon becomes negative. Note that at low advance ratio ($mu < 0.1$), for the cases investigated, the duct contributes more propulsion than the propeller. However, the duct thrust drops quicker with increasing advance ratio, and is soon over taken by the propeller thrust, indicating the deficiency of the duct at high advance ratio.

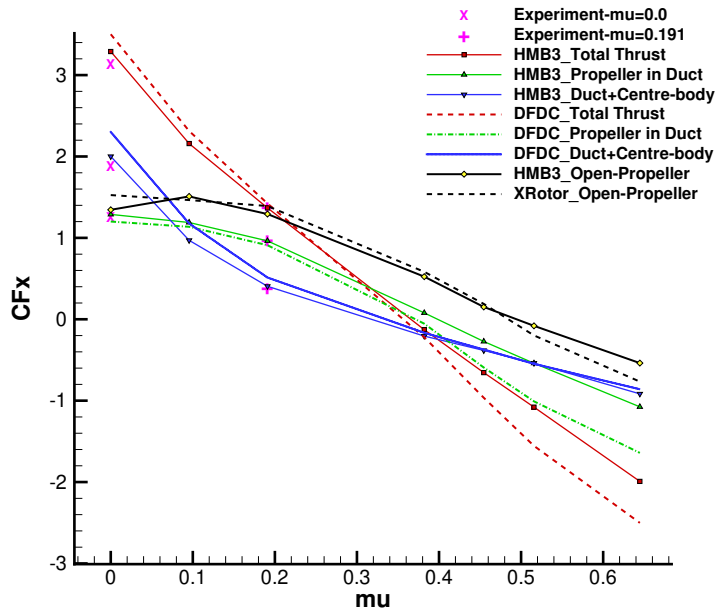

Fig. 21 Ducted and un-ducted propellers thrust at increasing advance ratios (all loads normalised by the free-stream speed at $\mu = 0.191$ for comparison).

The same advance ratios are also applied to the un-ducted propeller using both HMB3 and XRotor calculations. The agreement is good at low advance ratios, while slight discrepancies can be seen at high advance ratios. The same trend can be observed for the ducted propeller calculations. This can be attributed to the fact that at the high advance ratios studied, the local angles of attack for the blade elements become negative and the blade mostly works near stall conditions. Due to the duct induced inflow, as mentioned in Section III, the ducted propeller experiences more severe stall conditions, and the difference between the DFDC and HMB3 results is larger. While predictions for the duct force remain in good agreement at high advance ratios.

The un-ducted propeller is able to produce only half of the thrust the ducted counter-part is capable of producing. As the advance ratio increases, the un-ducted propeller thrust decreases following the similar trend as the propeller in the duct. Meanwhile, the total thrust of the ducted propeller drops faster due to the increasing duct drag, and is overstepped by the un-ducted propeller at around $\mu = 0.2$. This suggests again the problems of using a duct at high advance ratios.

The azimuth-averaged duct surface pressure distributions from HMB3 simulations are presented in Figures 22(a) to 22(c), along with the DFDC results for comparison. Favourable agreement between the methods is again noted at variable advance ratios. The pressure force vectors on the duct surface are also extracted from HMB3 results. It is clearly shown that the duct leading edge provides a significant suction force in hover ($\mu = 0.0$). As the advance

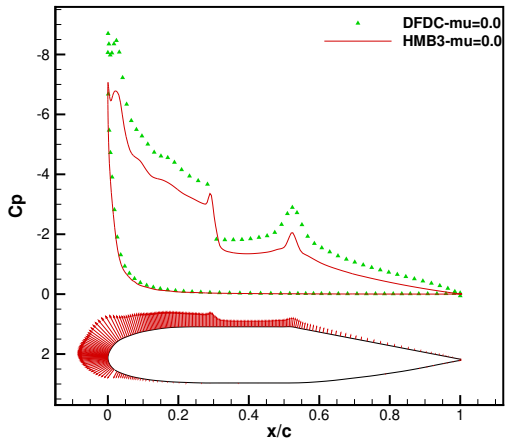

(a) Azimuth-averaged duct surface pressure distribution at $\mu = 0.0$.

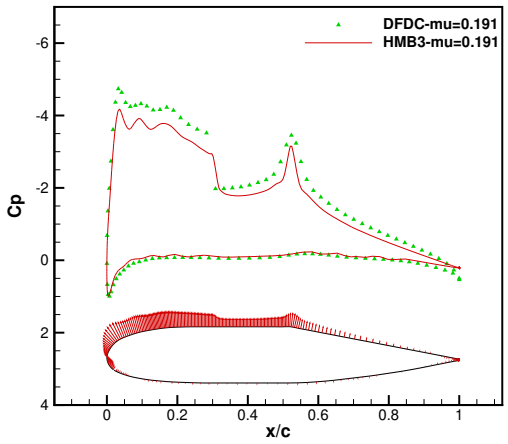

(b) Azimuth-averaged duct surface pressure distribution at $\mu = 0.191$.

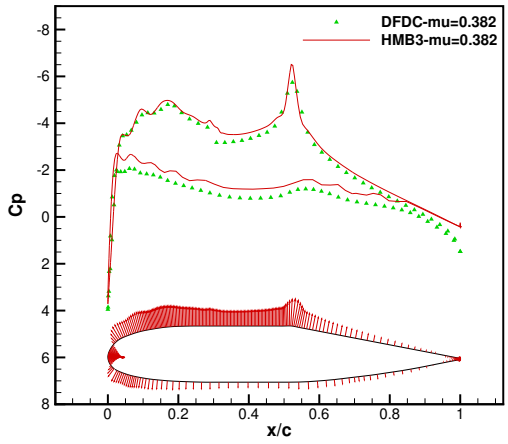

(c) Azimuth-averaged duct surface pressure distribution at $\mu = 0.382$.

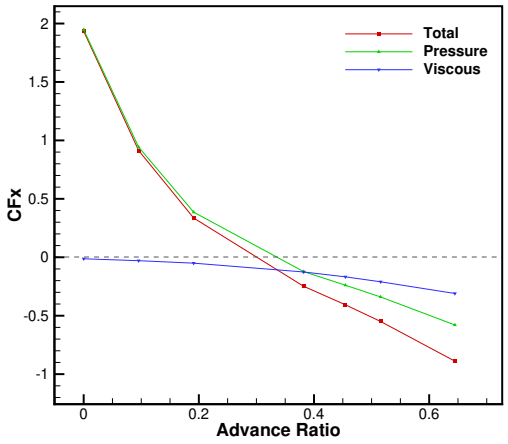

(d) Duct pressure and viscous forces breakdown at increasing advance ratios.

Fig. 22 Comparisons of duct surface pressure distributions (azimuth averaged) at low, medium, and high advance ratios, using HMB3 and DFDC calculations. Surface pressure force vectors are extracted from HMB3 simulations.

ratio increases, the pressure force on the outboard side of the leading edge gradually becomes negative. This region of negative forces grows and moves slowly inboard as the advance ratio is further increased, and a net drag on the duct increases. As the free-stream speed grows, the pressure jump imposed by the rotor disk is no longer the dominant flow feature. The diffuser exit still works, but the region producing drag force is also increasing. At $\mu = 0.382$ as in Figure 22(c), pressure forces on the duct outer surface are not to be ignored. Contributions of pressure and viscosity are given in Figure 22(d). The major component has always been due to pressure, but the viscous part, which always contributes to the drag, also grows slightly with the advance ratio.

Overall, the duct shows high efficiency at low and moderate advance ratios. However, the benefits diminish with growing advance ratios. Nevertheless, modifications can be made to the duct outer surface, especially near the inlet leading edge, to improve the duct performance particularly at high advance ratios. The duct chord length may also be shortened to reduce the viscous drag.

C. Ducted Propeller Performance at Cross-wind Conditions

Non-axial inflow for the ducted propeller may result in imbalanced aerodynamic forces and moments for both the duct and the propeller disk. Flow separation at the inlet or the downstream outer surfaces may also be encountered, depending on the propeller induction, the free-stream speed, the angle of attack, and the duct shape etc. To evaluate the performance at cross-wind, the high AoA conditions tested by Grunwald and Goodson [8] are simulated using HMB3 and presented here. The DFDC code, however, is not able to account for non-axial conditions.

The aerodynamic load variations with increasing angles of attack are presented in Figure 23. The simulations are performed at $AoA = 20°$ and $AoA = 50\circ$. Unsteady scale-adaptive simulations (SAS) are utilised, because of the possibly massive separation on the duct surface.

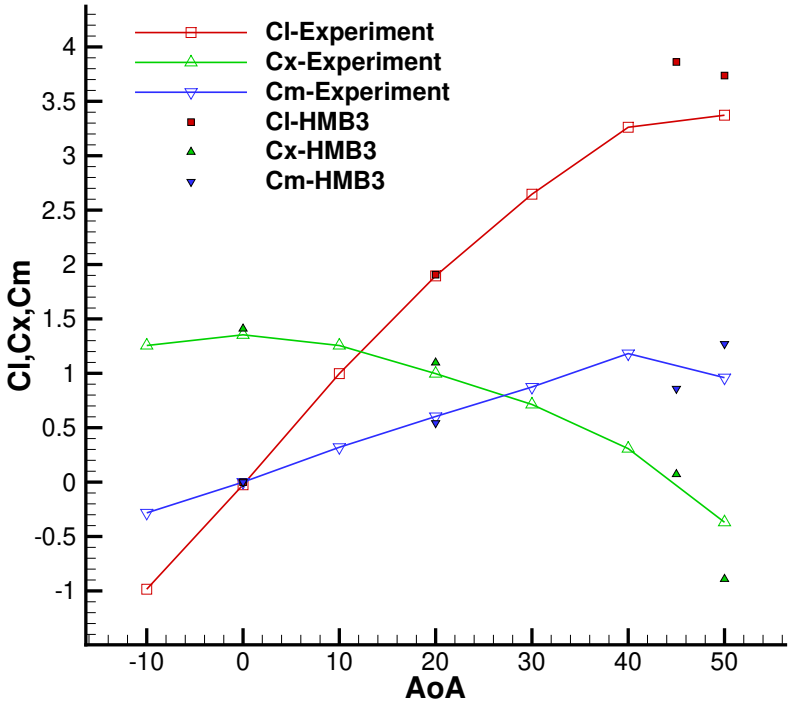

Fig. 23 Aerodynamic loads on the Grunwald ducted propeller working at high AoA conditions.

Good correlations for the total aerodynamic loads (averaged over revolutions) between the HMB3 and experimental data can be noticed in Figure 23. The separation on the duct surface, both inner and outer surfaces, is found to be delayed comparing to the empty duct without the propeller [8], thanks to the propeller suction. The aerodynamic loads show a linear response to the increasing AoA up to around $AoA = 40°$. Such high angles of attack are hardly encountered in axial flight, but may be encountered in transition and hover modes.

Table 7 Aerodynamic load breakdown for the Grunwald ducted propeller [8] at $AoA = 20°$.

	C_l	Contribution	C_{F_x}	Contribution	C_m(pitching)	Contribution
Total	1.922	-	1.096	-	0.553	-
Duct	1.483	77.17%	0.120	10.96%	0.500	90.51%
Propeller	0.405	21.09%	0.923	84.25%	0.053	9.50%

The breakdown of aerodynamic loads on the ducted propeller at $AoA = 20°$ are presented in Table 7. At the incidence of 20°, the ducted propeller generates a total force significantly higher than in the axial condition, of which the lift component is twice as much as the propulsion. A nose-up pitching moment is also resulted. As shown in Table 7, the duct claims the most contributions to the lift and the nose-up pitching moment, while the propeller contributes the most to the forward propulsion. It is therefore possible to use the duct as an annular wing for lift while producing also thrust. The centre-body has only some effects for the case analysed.

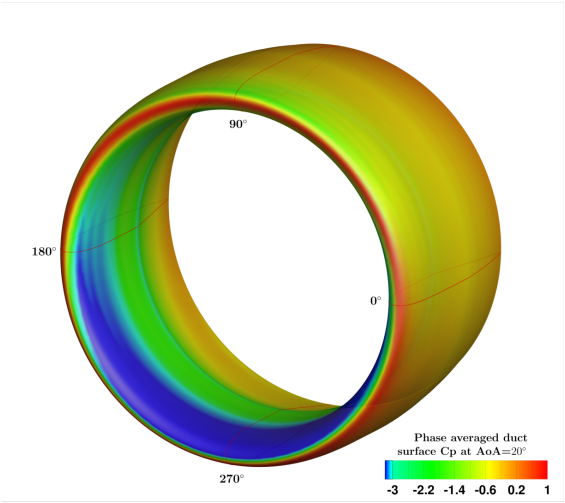

(a) Phase averaged duct surface pressure coefficient contours for the Grunwald ducted propeller at $AoA = 20°$.

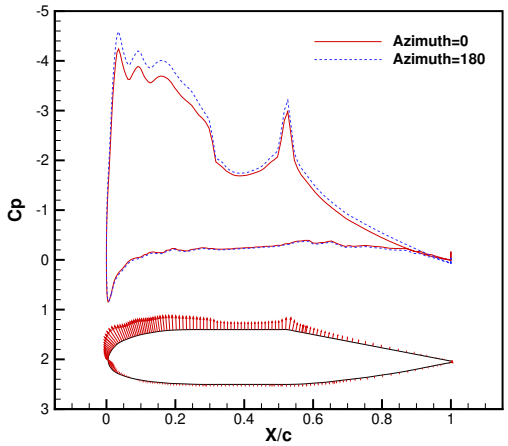

(b) Sectional pressure coefficient and vector distributions at 0° and 180° azimuth at $AoA = 20°$.

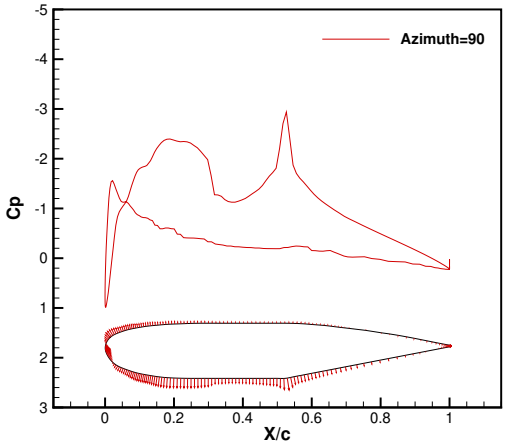

(c) Sectional pressure coefficient and vector distributions at 90° azimuth at $AoA = 20°$.

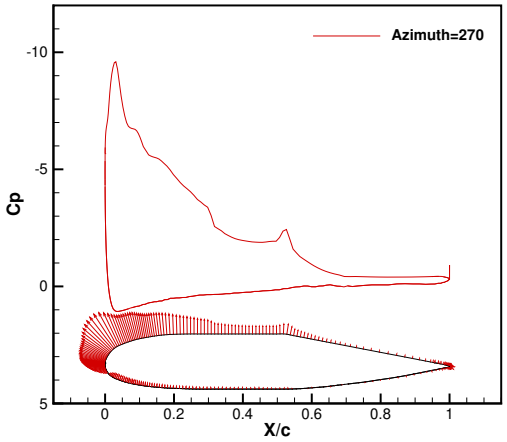

(d) Sectional pressure coefficient and vector distributions at 270° azimuth at $AoA = 20°$.

Fig. 24 Phase averaged duct surface Cp contours and vectors for the Grunwald [8] ducted propeller at $AoA = 20°$.

The duct surface pressure is extracted and averaged over revolutions, as presented in Figures 24(a) to 24(d). The surface pressure coefficient contours are presented in Figure 24(a). With the cross-wind coming from the 270° azimuth, a large region of low pressure can be noticed near the upstream (from 180° to 0° azimuth) inlet lip. The downstream lip sees generally higher pressure, as the stagnation area are moved more inboard. Sectional pressure coefficients and force vectors for the 0° and 180° azimuth are calculated and presented in Figure 24(b). The pressure distributions at these two sections are almost identical, with only small differences seen at the inner leading-edge regions. The duct has slightly lower pressure at the rotor advancing side (180° azimuth). Large differences can be noted, however, for the 90°

and 270° sections, as shown in Figures 24(c) and 24(d) respectively. The upstream section (270°) produces a large leading-edge suction on the inner surface. Whereas for the downstream section (90°), the leading-edge stagnation is moved more inboard due to the sideways flow and milder suction can be noticed on the outer surface. In this light, asymmetric geometric modifications can be made to the up- and downstream lips to accommodate local flow conditions.

To investigate the working condition of the propeller inside the duct at cross-wind, the axial velocity profile right before the rotor disk, extracted from the empty duct simulation at the same incidence of 20°, is shown in Figure 12(b). The propeller sees an imbalanced axial inflow, with the maximum at the up-stream lip about 50% larger than the minimum value at the down-stream lip. The phase-averaged axial and tangential propeller induced velocities are extracted and presented in Figures 25(a) and 25(b), respectively. The induction factor is defined as $IF = \frac{V_i}{V_\infty}$, where V_i is the propeller induced velocity subtracted from baseline flows(the empty duct at $AoA = 20°$ in Figure 12(b)). The axial induction factor is calculated using only the axial component of the induced velocity, while the tangential induction factor uses the tangential component.

An azimuthal shift of about 45° following the blade rotation (counter-clockwise) can be observed for both induction factors. Similar phenomena are reported in the study [29] of un-ducted propellers at yaw. The maximum axial induction is seen near the blade tip between 0° and 90° azimuth, while the minimum is near the root between 180° and 270°. Comparing to the open propeller study [29], the maximum values move further outboard towards the blade tip and the inner duct surface. Further, a concentric pattern can be noticed in Figure 25(a) for the axial induction, indicating a more azimuthally even distribution of the axial induced velocity. As for the tangential induction (Figure 25(b)), an inverted symmetric pattern is noted. The maxima and minima appear near the blade root and the centre-body surface, with an azimuthal shift by about 45°. In addition, the tangential values are about an order smaller than the axial component.

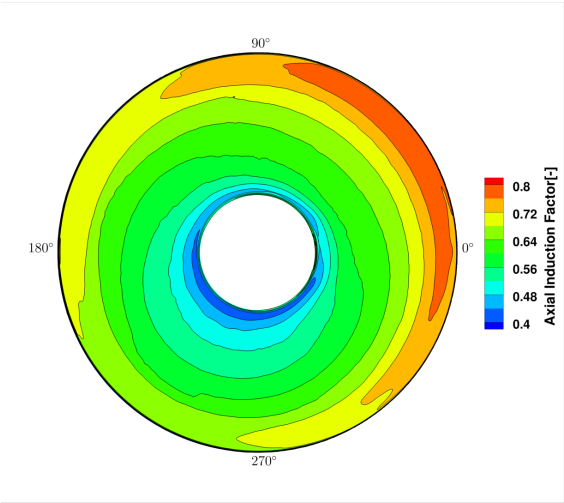

(a) Axial induction factor for the Grunwald ducted propeller at $AoA = 20°$.

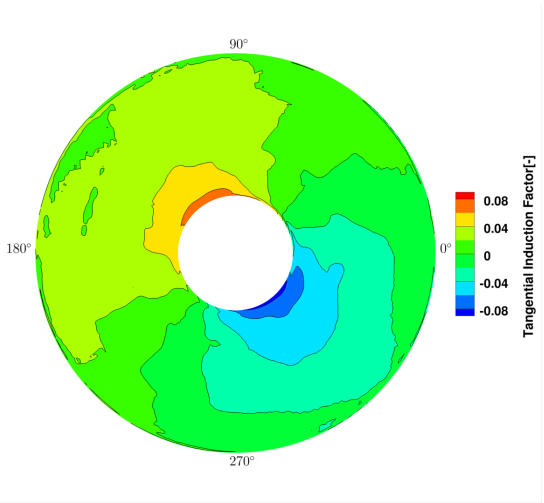

(b) Tangential induction factor for the Grunwald ducted propeller at $AoA = 20°$ (positive values are flowing towards the blade element).

Fig. 25 Axial and tangential propeller induction for the Grunwald ducted propeller at $AoA = 20°$.

Normal force distributions on the propeller disk at $AoA = 0°$ and 20° are presented in Figures 26(a) and 26(b), respectively. At $AoA = 20°$ as in Figure 26(b), the propeller normal force distribution sees combined effects of the axial and tangential inductions shown in Figures 25(a) and 25(b). The thrust distribution on the outboard of the propeller disk follows mostly the axial induction as in Figure 25(a), with the maximum appears on the advancing side between the 0° and 90°. While the inboard region sees a stronger effect from tangential induction. Comparing to the axisymmetric thrust distribution at $AoA = 0°$ in Figure 26(a), the propeller at $AoA = 20°$ produces imbalanced forces and moments similar to a helicopter rotor in forward flight.

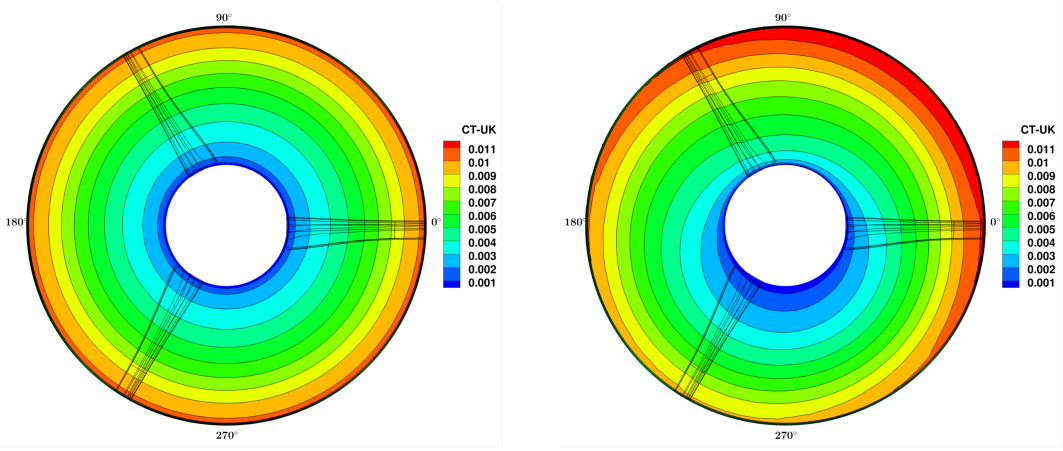

(a) Propeller disk normal force distribution at $AoA = 0°$.

(b) Propeller disk normal force distribution at $AoA = 20°$.

Fig. 26 Propeller disk normal force distributions at $AoA = 0°$ and $AoA = 20°$.

Conclusions

A tool chain development for the high-fidelity analysis of compound rotorcraft is described and validated for several ducted propeller cases. Performance analyses of the ducted propeller at various working conditions are presented. The following conclusions can be derived from this work:

1) The proposed automation framework is able to significantly accelerate the analysis process. The time needed for pre-processing is reduced to minutes from hours. The framework can accommodate variable shapes effectively and produce grids with high quality. Further development will be carried out to improve the robustness, versatility, and simplicity.
2) Simulations of ducted propellers using methods of different fidelity levels using grids generated by the automation framework are performed. Good agreement can be noticed between the high fidelity CFD simulations using the HMB3 solver, the experimental data, and lower-order predictive methods. The DFDC, XRotor, and HMB3 MRF methods are efficient in hover and axial flight simulations. The non-axial and unsteady conditions are resolved with accuracy using the HMB3 solver with the complete configurations.
3) The superior performance of the ducted propeller at low or medium advance ratios are confirmed. The performance gain is specified as from the duct. The propeller inside the duct sees a higher baseline axial velocity due to the induction of the duct. At high advance ratios, however, the duct becomes deficient due to the drag. At moderate incidences, the duct produces a large lift force and a nose-up pitching moment. Also, the propeller experiences imbalanced inflow velocities.

Future work will investigate the sensitivity of flow to geometry and carry out optimisation of duct shapes to improve the high speed performance. Asymmetric duct shapes at cross-wind are also to be investigated and evaluated.

Acknowledgments

The sponsorship of the University of Glasgow and the China Scholarship Concil is gratefully acknowledged.

References

[1] Graham, J., "Definition of a Rotorcraft," `https://www.aerosociety.com/Assets/Docs/Publications/SpecialistPapers/Definition_of_a_Rotorcraft.pdf`, Februry 2013. Special paper of the Royal Aeronautical Society, available on-line.

[2] Brouwers, E., Fillman, M., and Deresz, R., "ADVANCED AH-64 COMPOUND WIND TUNNEL TESTING OVERVIEW," *Proceedings of the 75th Annual Forum*, 2019.

[3] Constantin Öhrle, M. K. E. K., Ulrich Schaferlein, "Higher-order Simulations of a Compound Helicopter using Adaptive Mesh Refinement," *the AHS International 74th Annual Forum & Technology Display, Phoenix, Arizona, USA*, 2018.

[4] Jakob Thiemeier, F. F. M. K. E. K., Constantin Öhrle, "AERODYNAMIC AND FLIGHT MECHANICS ANALYSIS OF AIRBUS HELICOPTERS' COMPOUND HELICOPTER RACER IN HOVER UNDER CROSSWIND CONDITIONS," *44th European Rotorcraft Forum, Delft, The Netherlands*, 2018.

[5] Ohrle, C., Frey, F., Thiemeier, J., Kebler, M., Kramer, E., Embacher, M., Cranga, P., and Eglin, P., "Compound helicopter X^3 in high-speed flight: correlation of simulation and flight test," *75th Annual Forum and Technology Display*, 2019.

[6] Johnson, W., Elmore, J., Keen, E., Gallaher, A., and Nunez, G., "Coaxial compound helicopter for confined urban operations," 2016, pp. 210–239.

[7] Hubbard, H. H., "Sound measurements for five shrouded propellers at static conditions," Tech. rep., National Advisory Committee for Aeronautics, 1950.

[8] Grunwald, K. J., and Goodson, K. W., "Aerodynamic loads on an isolated shrouded-propeller configuration for angles of attack from -10 degrees to 110 degrees," Tech. rep., National Aeronautics and Space Administration Washington DC, 1962.

[9] Steijl, R., Barakos, G. N., and Badcock, K., "A framework for CFD analysis of helicopter rotors in hover and forward flight," *International Journal for Numerical Methods in Fluids*, Vol. 51, No. 8, 2006, pp. 819–847.

[10] Steijl, R., and Barakos, G. N., "Sliding mesh algorithm for CFD analysis of helicopter rotor-fuselage aerodynamics," *International Journal for Numerical Methods in Fluids*, Vol. 58, No. 5, 2008, pp. 527–549.

[11] Biava, M., Woodgate, M., and Barakos, G. N., "Fully implicit discrete-adjoint methods for rotorcraft applications," *AIAA Journal*, Vol. 54, No. 2, 2015, pp. 735–749.

[12] Osher, S., and Chakravarthy, S., "Upwind schemes and boundary conditions with applications to Euler equations in general geometries," *Journal of Computational Physics*, Vol. 50, No. 3, 1983, pp. 447–481.

[13] van Leer, B., "Towards the ultimate conservative difference scheme. V. A second-order sequel to Godunov's Method," *Journal of Computational Physics*, Vol. 32, No. 1, 1979, pp. 101–136.

[14] van Albada, G. D., van Leer, B., and Roberts, W. W., "A Comparative Study of COmputational Methods in Cosmic Gas Dynamics," *Astronomy and Astrophysics*, Vol. 108, No. 1, 1982, pp. 76–84.

[15] Axelsson, O., *Iterative Solution Methods*, Cambridge University Press, 1994.

[16] Menter, F., "Two-Equation Eddy-Viscosity Turbulence Models for Engineering Applications," *AIAA Journal*, Vol. 32, No. 8, 1993, pp. 1598–1605.

[17] Babu, S. V., Zografakis, G., Barakos, G. N., and Kusyumov, A., "Evaluation of scale-adaptive simulation for transonic cavity flows," *International Journal of Engineering Systems Modelling and Simulation*, Vol. 8, No. 2, 2016, pp. 106–124.

[18] Loupy, G., Barakos, G. N., and Taylor, N. J., "Multi-disciplinary simulations of stores in weapon bays using scale adaptive simulation," *Journal of Fluids and Structures*, Vol. 81, 2018, pp. 437–465.

[19] Higgins, R., Jimenez-Garcia, A., Barakos, G. N., and Bown, N., "A Time-Marching Aeroelastic Method Applied to Propeller Flutter," *AIAA Scitech 2019 Forum*, 2019, p. 1102.

[20] Jarkowski, M., Woodgate, M., Barakos, G., and Rokicki, J., "Towards consistent hybrid overset mesh methods for rotorcraft CFD," *International Journal for Numerical Methods in Fluids*, Vol. 74, No. 8, 2014, pp. 543–576.

[21] Woodgate, M. A., and Barakos, G. N., "Comparison between different grid methodologies for rotorcraft configurations," *41st European Rotorcraft Forum, Munich, Germany, 1-4 September, 2015*, 2015, p. 133.

[22] Biava, M., and Barakos, G. N., "Optimisation of ducted propellers for hybrid air vehicles using high-fidelity CFD," *The Aeronautical Journal*, Vol. 120, No. 1232, 2016, pp. 1632–1657.

[23] Drela, M., and Youngren, H., "XROTOR user guide," `http://web.mit.edu/drela/Public/web/xrotor/`, 2003. Available on-line.

[24] Youngren, H., Drela, M., and Sanders, S., "Ducted Fan Design Code," http://web.mit.edu/drela/Public/web/dfdc/, December 2005. Ducted Fan Design Code homepage, available on-line.

[25] Drela, M., and Youngre, H., "Axisymmetric Analysis and Design of Ducted Rotors," http://web.mit.edu/drela/Public/web/dfdc/DFDCtheory12-31.pdf, December 2005. Ducted Fan Design Code theory, available on-line.

[26] Fletcher, H. S., "Experimental investigation of lift, drag, and pitching moment of five annular airfoils," Tech. rep., NACA-TN-4117, 1957.

[27] Kruger, W., "On wind tunnel tests and computations concerning the problem of shrouded propellers," Tech. rep., National Advisory Committee for Aeronautics, 1949.

[28] Abrego, A. I., Bulaga, R. W., and Rutkowski, M., "Performance study of a ducted fan system," *the American Helicopter Society Aerodynamics, Acoustics, and Test and Evaluation Technical Specialists Meeting, San Francisco, CA*, 2002.

[29] Higgins, B. G., R.J., and Green, R., "Numerical Investigation of a Two-Bladed Propeller Inflow at Yaw," *Journal of Aircraft*, 2019.